Some Use Cases for Composite Finite Elements in Image Based Computing

Lars Ole Schwen[1], Torben Pätz[1], and Tobias Preusser[1,2]

[1] Fraunhofer MEVIS, Bremen, Germany
[2] Jacobs University Bremen, Germany
{ole.schwen,torben.paetz,tobias.preusser}@mevis.fraunhofer.de

Abstract Many bio-medical simulations involve structures of complicated shape. Frequently, the geometry information is given by radiological images. A particular challenge for model discretization in this context is generating appropriate computational meshes.
One efficient approach for Finite Element simulations avoiding meshing is the Composite Finite Element (CFE) approach that has been developed and implemented for image-based simulations during the past decade. In the present paper, we provide an overview of previous own work in this field, summarizing the method and showing selected applications: simulation of radio-frequency ablation including vaporization, simulation of elastic deformation of trabecular bone, and numerical homogenization of material properties for the latter.

[published in MICCAI 2015 Workshop Proceedings "Computational Biomechanics for Medicine X", pp. 128–140.]

1 Introduction

In the past decades mathematical modeling, simulation, and optimization have become indispensable tools in systems biology, systems medicine, as well as medical diagnosis and treatment-planning. In the 'image based computing' paradigm, radiological images like CT, MRI, ultrasound, etc. are analyzed to yield segmented structures of organs, tissue, or other structures pictured. The consequent goal is to simulate physiological processes, or to simulate and optimize treatments using mathematical models and their numerical implementations. A particular challenge in this is, however, the generation of computational meshes from the segmented imaging data that is needed in the process of discretization of models.

In fact, structures in organisms have a complicated geometry. They are in general irregularly shaped and show large intra- and inter-individual variations. Moreover, it is often necessary to also resolve internal sub-structures or interfaces with a computational mesh, thus to account for various bio-physical properties of the many tissue-types that might be involved and which may be discontinuous at the internal tissue interfaces. These facts make mesh generation for image based computing a difficult task that, moreover, must respect constraints of a clinical workflow in case of a true medical application in daily routine.

For the discretization of mathematical models that are characterized by partial differential equations (PDEs) computational meshes are directly related to the Finite Element spaces spanning the space of solutions. In the case of irregular boundaries or internal structures, it is known that the solutions have less regularity that may result, e.g., in kinks and discontinuous gradients. The straightforward approach to tackle these irregularities is mesh adaptivity, i.e., decreasing the size of the mesh's cells in areas with lower regularity of the solution and thus adapting the associated Finite Element spaces. Other approaches avoiding mesh adaptivity that have been discussed in the literature include generalized FEM (GFEM), extended FEM (XFEM), Immersed FEM, Fictitious Domain Methods, WEB-Splines, and others. We refer to [19, 21, 26] for literature overviews and [4, 7, 8, 13, 17, 18, 25] for selected more recent approaches.

In this paper we review the Composite Finite Element (CFE) approach to image based computing. The CFE approach goes back to [10, 24]. This paper is a summary of our work from the past decade orginally published in [19, 21–23, 26–30, 35]. The method works efficiently on regular hexahedral grids as they are provided by the usual three-dimensional voxel grids of medical images. Still it allows for the resolution of complicated geometries and interfaces by automatically adapting standard linear Finite Element basis functions and thus modifying the corresponding Finite Element space accordingly. In the remainder of the paper we first explain the general idea of CFE in more detail in Section 2 and an approach for numerical homogenization in Section 3. Then, in Section 4, we show two applications from the field of medical image computing that demonstrate the use of CFE: the simulation of radio-frequency ablation, the simulation of the elastic deformation of vertebral trabecular bone, and numerical homogenization for the latter. We close the paper with a summary and conclusions in Section 5.

2 Composite Finite Elements

We will describe the concept of CFE for the domain $\Omega = (0, 1)^3$, which is be discretized with a regular hexahedral grid $\mathcal{G}$ that has 2^{3l} elements of grid width $h = 2^{-l}$ and a total of $(2^l + 1)^3$ nodes. We choose to work with the unit cube here as it eases the presentation. The application of CFE to other cuboid domains is of course possible straightforwardly. Working with piecewise affine-linear basis functions, we subdivide each hexahedron in six tetrahedra in such a way that edges are consistent with neighboring elements, resulting in the mesh $\mathcal{G}^{\boxtimes}$ denoted as the regular tetrahedral mesh.

We assume that the domain Ω contains $\Omega_i \subset \Omega$, the object we are interested in, and which has a complicated boundary. Consequently the solution to an elliptic (or parabolic) PDE will be supported on Ω_i and we will build a Finite Element space whose basis functions are supported on Ω_i. If in addition the object comprises complex interfaces between materials of different bio-physical properties the solution to the PDE will have kinks at the interface. Such kinks result from discontinuities of material properties when they have different values on both sides of the interface. The material properties enter the equations as

coefficients (e.g., as diffusivities or elasticity parameters) and the kink in the solution will depend on the ratio of the material property across the interface. Again, in CFE we will build basis functions that are able to interpolate functions fulfilling the kink condition. This approach to complex object boundaries and interfaces makes classical grid adaptivity obsolete.

To proceed let us assume that $\overline{\Omega} = \overline{\Omega_i \cup \Omega_e}$ and further $\overline{\Omega_i} = \overline{\Omega_+ \cup \Omega_-}$ where $\Omega_\pm$ are disjoint sets. Thus, the domain Ω is decomposed into the object Ω_i and its exterior Ω_e. The object Ω_i contains two material domains $\Omega_\pm$. A generalization to more objects and more materials is of course easily possible [27]. In image based computing it is convenient to define these domains from 3D image data that is provided on a regular hexahedral voxel grid. With image processing methodology level-set functions can be provided such that the zero level-sets define the interfaces of the domains, see below.

In the following we will describe how to construct CFE for complicated domains, for complicated interfaces between different materials, and how to use CFE in the context of homogenization. Note that our expositions will be brief and just explaining the principal concepts. For more details we refer the reader to the original publications that mentioned the respective sections below.

The treatment of different cases of boundary conditions (Dirichlet and Neumann; on the bounding box and on the interface; zero and nonzero) is addressed in [27]. A key advantage of the underlying uniform hexahedral grids is their natural hierarchy of coarse scales. These were used in a CFE multigrid solver for the case of complicated domains [19]. Defining a suitable coarsening scheme for CFE for discontinuous coefficients turned out to be challenging [21] and requires further investigation. One possibility could be a hybrid approach combining standard geometric, algebraic [33], and topological [6] coarsening.

2.1 CFE for Complicated Domains

Let us first consider the case of a domain with complicated boundary consisting of only a single material, w.l.o.g. described by $\Omega_+ = \emptyset$ and $\Omega_i = \Omega_-$. The interior boundary is then given as $\Gamma = \partial\Omega_i \cap \Omega$. Let $\varphi\colon \Omega \to \mathbb{R}$ be the level-set function defining this domain, i.e., a function whose zero sub-levelset is Ω_-.

In this case, CFE basis functions are constructed to be standard affine FE basis functions restricted to Ω_i as shown in Fig. 1 for the 2D case. This construction is achieved by introducing an auxiliary mesh $\mathcal{G}^{\triangle}$. For this purpose, tetrahedra of $\mathcal{G}^{\boxtimes}$ intersected by the interior boundary Γ are further subdivided in four or six sub-tetrahedra such that the a linear approximation to the boundary Γ is resolved. In fact, the auxiliary nodes $n_i^{\triangle}$ needed for the construction of the auxiliary mesh are computed as the zero crossings of the affine-linear interpolation of φ on the edges of $\mathcal{G}^{\boxtimes}$ that are intersected by Γ. From the standard, piecewise affine basis functions $\mathcal{G}^{\triangle}$, CFE basis functions are composed as a weighted sum, where the weights are given by the barycentric coordinates of the auxiliary nodes $n_i^{\triangle}$ on the respective edges of $\mathcal{G}^{\boxtimes}$.

For a detailed discussion of the CFE construction including the description of a multigrid solver, we refer to [19, 26].

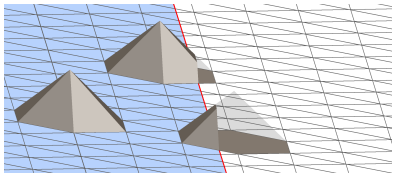

Figure 1. 2D CFE Basis Functions for Complicated Domains. For the domain (*left*, light blue region), CFE basis functions in the interior are standard piecewise affine tent functions for the nodes of the regular tetrahedral mesh $\mathcal{G}^{\boxtimes}$. For the exterior (*right*, white region), there are no degrees of freedom and no basis functions. Near the interface (red line), standard tent functions are restricted to the interior of the domain. This applies to the nodes of $\mathcal{G}^{\boxtimes}$ adjacent to the intersection of the interface. (Figure from [26, Fig. 3.11])

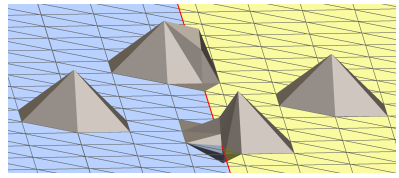

Figure 2. 2D CFE Basis Functions for Complicated Interfaces. For piecewise constant coefficients in two domains (light blue and yellow regions) with a discontinuity across the interface (red line), CFE basis functions far from the interface are again standard piecewise affine tent functions for the nodes of the regular tetrahedral mesh $\mathcal{G}^{\boxtimes}$. At the interface, CFE basis functions are constructed in such a way that they can interpolate the local kink condition, in this case for isotropic scalar coefficients with a ratio of $1:10$. These CFE basis functions at the interface may attain values outside $[0,1]$ and may have extended support. Still, they form a partition of unity and their support remains local and bounded. (Figure from [26, Fig. 3.12])

2.2 CFE for Discontinuous Coefficients

For the case of discontinuous coefficients, let us assume that $\Omega = \Omega_i$, i.e., there is no additional complicated domain boundary. In this case, let $\Gamma = \partial\overline{\Omega_+} \cap \partial\overline{\Omega_-}$, i.e., the interface between the two different materials, and let again $\varphi\colon \Omega \to \mathbb{R}$ be the function defining this interface, i.e., φ is positive/negative in $\Omega_\pm$ and Γ is its zero levelset.

In this case, CFE basis functions are constructed such that they are capable of interpolating functions satisfying the kink condition due to the parameter discontinuity (denoted below as 'admissible' functions). The construction starts similar to the case above, introducing $\mathcal{G}^{\boxtimes}$ which now approximates the interface between two material domains. Next, composition weights need to be determined to to obtain CFE basis functions as weighted sums of standard, piecewise affine basis functions $\mathcal{G}^{\triangle}$. For this purpose, we consider the problem of locally interpolating admissible functions at nodes $n_i^{\triangle}$ of the auxiliary mesh $\mathcal{G}^{\triangle}$ from nodes $n_j^{\boxtimes}$ of $\mathcal{G}^{\boxtimes}$. The admissibility condition (= kink condition) involves the local interface geometry, the underlying PDE, and the values of its coefficients on both sides of the interface. Using a Taylor expansion, known properties can be exploited, namely continuity of *(a)* the function, of *(b)* its derivative in tangential directions, and of *(c)* coefficient times derivative in normal direction of the function. Averaging over all adjacent tetrahedra of $\mathcal{G}^{\boxtimes}$ provides the interpolation weight $w_{i,j}$ for the pair $\left(n_i^{\triangle}, n_j^{\boxtimes}\right)$. In turn, $w_{i,j}$ is finally used as the composition

weight with which the auxiliary basis function for $n_i^{\triangle}$ of $\mathcal{G}^{\triangle}$ contributes to the CFE basis function for $n_j^{\boxtimes}$ of $\mathcal{G}^{\boxtimes}$.

For diffusion as a scalar model problem, a 2D example is shown in Fig. 2. The resulting basis functions remain a partition of unity and retain boundedness of their supports. However, they may attain values below 0 (see Fig. 2) or greater than 1 near the interface.

In case of vector-valued elasticity with discontinuous material parameters, the construction is more technical as the coupling condition at the interface then involves three dimensions simultaneously. For nodes near the interface, this leads to three CFE basis functions, each of which has contributions in all three space dimensions. For a more detailed description of the construction for the scalar and vector-valued model problems, we refer to [21, 26].

3 Numerical Homogenization with CFE

Being specifically designed for simulations on cuboid domains, CFE are well suited for numerical homogenization, i.e., for determining effective macroscopic material parameters. An approach for numerical homogenization for linear elasticity of trabecular bone specimens was presented in [23], other approaches include [9, 14]. The basic idea of our approach [23] is to simulate six cases of uniaxial compression and shearing ('macroscopic unit strains') and determine the respective stress response of a statistically representative cubic part of the trabecular bone. Together, this provides the necessary information for the macroscopic linear elasticity tensor.

3.1 Simulations on Representative Volume Elements.

In case of microstuctures with exact geometric periodicity, the 'cell problem' approach cf. [2, Chapter 1] could be applied. Here, one fundamental cell of the microstructure can be used as the computational domain, and the deformation due to macroscopic unit strains can be determined using periodic boundary conditions. The stress response can then be evaluated by integration over the entire fundamental cell.

As biological structures like, e.g., trabecular bone, do not have an exactly periodic geometric structure, there is no geometrically fundamental cell of the object on which to impose periodic boundary conditions. Thus, we modify the 'cell problem' approach and use a statistically representative part of the structure as the computational domain, which we call representative volume element or RVE [15]. For simplicity, the RVE is assumed to be cube-shaped. Macroscopic unit strains are imposed by corresponding Dirichlet boundary conditions on the entire outer boundary of the RVE. Evaluating the stress response is then restricted to an inner part of the RVE sufficiently far from the outer boundary. This is necessary to avoid artificial stiffening due to boundary effects [21, Fig. 7.3]. A suitable thickness for the boundary layer omitted for the stress evaluation turned out to be [21, Section 7.2] approximately one eighth of the edge length of

the RVE. Based on [11, 34], the size of the interior used for stress evaluation was chosen to be at least 5 times the intertrabecular distance (pore size).

3.2 Macroscopic Linear Elasticity Tensors.

From the approach described above, the stress response for each unit strain is obtained, providing all parameters of the macroscopic elasticity tensor, i.e., the effective elasticity tensor.

For these, the question arises whether they are approximately orthotropic, and if so, what is the orientation of the axes. For this purpose, we solve an optimization problem, finding the rotation of the coordinate system for which the deviation of the tensor from an orthotropic one is minimized. The objective function representing this deviation is obtained from the tensor written in Voigt's notation where orthotropy is observed by certain entries being zero. Again, we refer the reader to [23] for more details on the approach.

4 Applications

In the following we will briefly describe some use cases for the CFE approaches described so far.

4.1 Vaporization during Radio-Frequency Ablation

As a first application reported in [20], we consider a simulation of radio-frequency ablation (RFA). RFA is a minimally invasive technique for the treatment of lesions, e.g., liver cancer [3, 16]. For RFA, a thin probe carrying electrodes is placed percutaneously inside the tumor and connected to an electric generator. Due to the electric resistance of the tissue, heat develops and destroys proteins and thus cells. When the temperature exceeds 100°C, the water inside the tissue vaporizes. This changes both the heat conductivity and the electric conductivity, and thus the electric potential causing the heating.

To simulate the temperature evolution during RFA, we couple models for electrostatic fields and temperature diffusion with a model for phase changes to account for the water evaporization. Thus, we have a free boundary problem with a complicated boundary that is coupled with discontinuous material coefficients across this interface. In the following, we discretize this problem with the CFE approach. In the notation introduced above, we consider the liquid phase to be 'the object' $\Omega_i = \Omega_l$ and the gaseous phase to be 'the exterior' $\Omega_e = \Omega_g$. Here and in the following, indices l denote quantities in the liquid phase, whereas the subscript g denotes quantities in the gaseous phase.

Phase Change. The phase change is modeled by a well-known Stefan problem [31] that describes the discontinuity of the temperature gradient across an interface between water in different phases, e.g., between liquid and vaporized water:

$$\frac{[-\lambda \nabla T \cdot N]}{L} = \rho_l \Big(v_l - D \Big) \ , \tag{1}$$

where λ is the the thermal conductivity, T the temperature, N the unit normal to the interface pointing from the liquid to the vapor domain, L the latent heat of the phase change, ρ_l the density of the liquid, v_l the liquid vapor speed at the interface and D the interface speed in normal direction. The jump operator $[A] := A_g - A_l$ denotes the difference between quantities on the liquid and vapor side of the interface. The Stefan condition allows to decouple the heat transfer equations in the liquid and vapor phase. Thus, for the heat diffusion we end up with the equations

$$\begin{aligned} \rho_g c_g \partial_t T + \rho_g c_g V \cdot \nabla T &= -\mathrm{div}(\lambda_g \nabla T) + Q_{\mathrm{rf}} \quad \text{in } \Omega_g \times \mathbb{R}^+, \\ \rho_l c_l \partial_t T &= -\mathrm{div}(\lambda_l \nabla T) + Q_{\mathrm{rf}} \quad \text{in } \Omega_l \times \mathbb{R}^+, \end{aligned} \tag{2}$$

with appropriate initial and boundary conditions and where Q_{rf} is the heat source according to the electric field caused by the RF current, see below. These equations, with complicated shaped domain boundary on the liquid-vapor boundary are discretized and solved using the CFE approach presented above. For details, we refer to [20].

RFA Simulation. The second main component of the RFA simulation is the solution of the electrostatic equation

$$-\mathrm{div}(\sigma \nabla \Phi) = 0 \text{ in } \Omega \tag{3}$$

with appropriate boundary conditions. This equation provides the electric potential and thus the heat source $Q_{\mathrm{rf}} = \sigma \|\nabla \Phi\|^2$. Here, σ is the electric conductivity that has a discontinuity at the interface separating liquid and gaseous domain.

Thus, for the overall RFA simulation, we need to solve *(a)* two heat transfer equations on the vapor and liquid domains domains of complicated shape, one for each phase, and *(b)* the potential equation for computing the electric potential with a discontinuous coefficient on the interface between the two domains. The evolution of the interface is obtained through the Stefan condition from above.

With this RFA model, we were able to calculate the expansion of a vapor bubble around the probe (see Fig. 3). With our simulation we achieve results comparable to measurements from ex situ experiments. Additionally, we computed the impedance during ablation in our simulations and compared them to measurements from [32, Fig. 7-1], see Fig. 4. Indeed, the characteristics of the curves for numerical simulation and experiment coincide, i.e., the impedance slightly decreases at the beginning; it rises steeply when the vapor bubble around the applicator is established; and the impedance remains constant afterwards.

4.2 Elastic Deformation of Trabecular Bone

Vertebroplasty. As an application involving linear elasticity with discontinuous coefficients, we consider an example from [21, 26], a specimen of a porcine T1 vertebral body virtually embedded in Polymethylmethacrylate (PMMA) subject to 1 % longitudinal compression. Material properties for the bone are

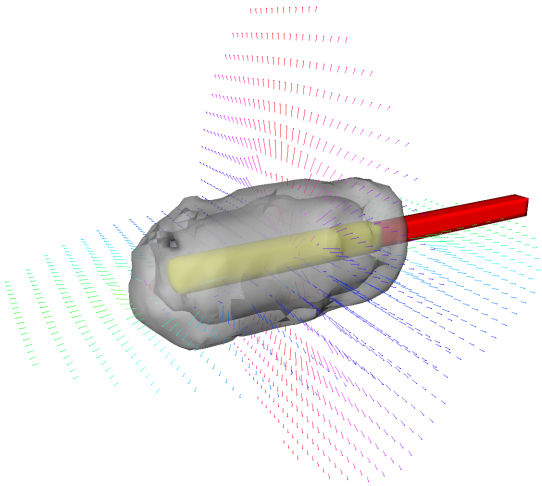

Figure 3. Expansion of the vapor phase around an RF probe. Arrows, color coded by velocity, indicate the vector field that drives the evolution of the interface, i.e., the water bubble. (Image from [20, Fig. 4.6]. Copyright © 2012 Society for Industrial Mathematics. Reprinted with permission. All rights reserved.)

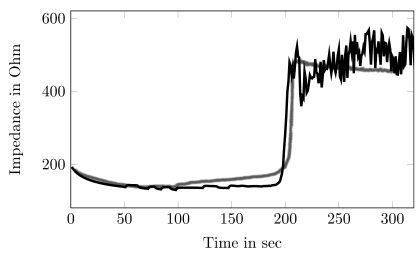

Figure 4. Comparison of the impedance measured during an ablation (grey curve, experimental data from [32]) and computed from the simulation (black curve). (Figure adapted from [20, Fig. 4.7]. Original image Copyright © 2012 Society for Industrial Mathematics. Reprinted with permission. All rights reserved.)

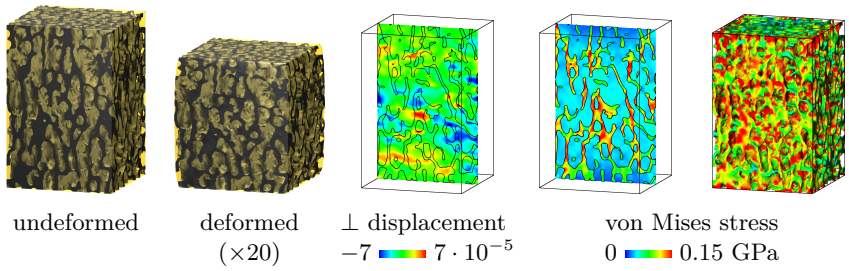

Figure 5. Vertebroplasty. For a porcine trabecular bone specimen virtually embedded in Polymethylmethacrylate (PMMA), compression was simulated. On a slice through the center of the specimen, the displacements perpendicular to the slice are shown in units relative to the specimen height. Moreover, the von Mises stress on that slice as well as the bone/PMMA interface are visualized. These visualizations show the impact of the parameter discontinuity across the interface of geometrically complicated shape. (Figure adapted from [26, Fig. 7.28] and [21, Fig. 6.5])

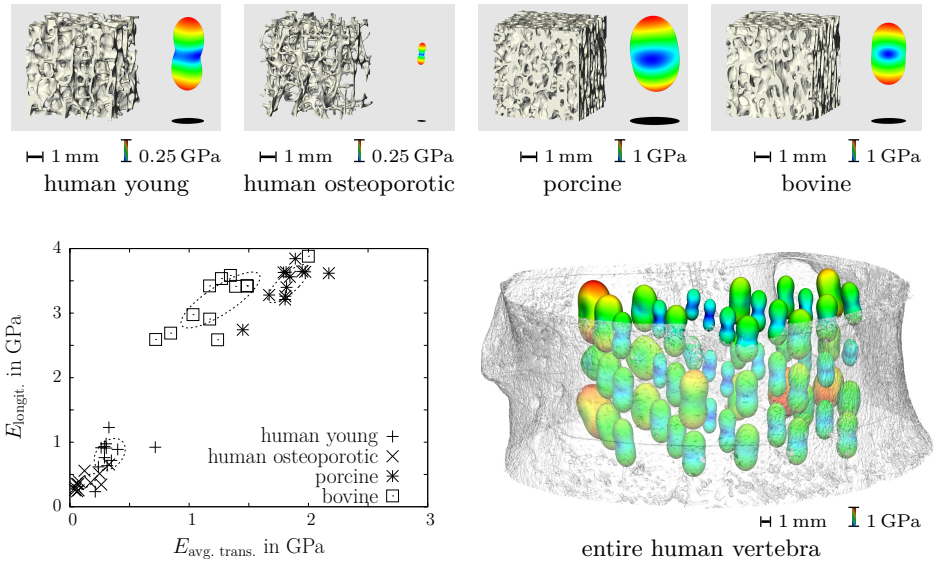

Figure 6. Comparison of Effective Elasticity Tensors. The four images in the *top row* show specimens from a human T12, from an osteoporotic human T10, a porcine T1 and a bovine L1 vertebra along with the effective elasticity tensors obtained by our numerical homogenization procedure (images adapted from [26, Fig. 7.36]). The overall stiffness matches the visual impression of the bone density, and the stiffness is largest in approximately the craniocaudal direction, corresponding to the vertical axis in the specimens. The *bottom left* plot provides a comparison of longitudinal stiffness and average stiffness in the transverse directions for multiple specimens of the species above (adapted from [23, Fig. 2]). This shows a rather clear clustering in terms of both absolute stiffness and ratio of longitudinal over transverse stiffness. The *bottom right* image comprises the effective elasticity tensors obtained for different positions within an entire human L4 vertebra (image adapted from [29, Fig. 6], original image Copyright © 2012 Taylor & Francis, http://www.tandfonline.com/), again showing craniocaudal anisotropy and stiffness variations depending on the position.

assumed to be those for human vertebral bodies, $E = 13\,\text{GPa}$ and $\nu = 0.32$ [36], and $E = 3\,\text{GPa}$ and $\nu = 0.38$ for PMMA as in [21]. With an isotropic image resolution of $35\,\mu\text{m}$, the resulting computational mesh had $143 \times 143 \times 214$ nodes. Results of this simulation are shown in Fig. 5.

Effective Elasticity Tensors of Trabecular Bone in Different Species. As a second application involving trabecular bone, we investigate differences in the macroscopic stiffness of specimens taken from vertebrae of different species [23]. For this purpose, cubic specimens of edge length 5.16 mm were obtained from a young male human, an osteoporotic female human, a porcine, and a bovine spine. The values above, $E = 13\,\text{GPa}$ and $\nu = 0.32$, were used as material properties for the trabecular bone, this time viewed as a complicated domain without surrounding

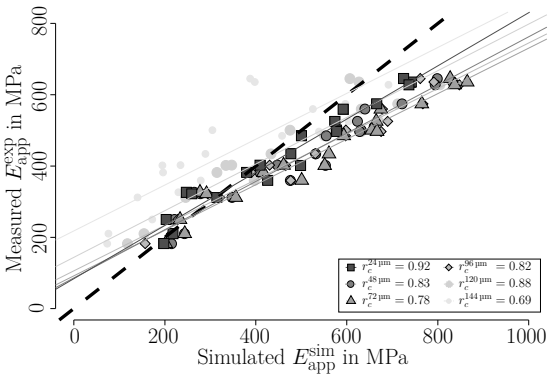

Figure 7. Correlations Between Experiment and CFE Homogenization. Correlations lines for resolutions below 168 µm were statistically significant ($p < 0.05$). Concordance coefficients r_c are given in the box for the varying resolutions. Ideal concordance would have been given by a correlation straight falling together with the black, dashed line. (Image adapted from [29, Fig. 3], original image Copyright © 2012 Taylor & Francis, http://www.tandfonline.com/)

medium. Using the numerical homogenization approach above, effective stiffness tensors were obtained for each of the specimens, visualized in Fig. 6.

Here, in order to give a quick visual impression of the macroscopic elasticity properties, we use the visualization presented in [5, 12]: A sphere is deformed according to the compressive stiffness in different directions, and it is rendered colored according to the respective bulk modulus, resulting in the colored 'peanuts' shown in Fig. 6.

Plotting the longitudinal and the average transverse stiffness for all specimens, a clear clustering of the different species can be observed. In [29], intravertebral variations were investigated further for multiple samples of an entire human vertebra, also shown in Fig. 6.

A validation of the CFE elasticity simulation and the homogenization has been discussed in [29]. There, local stiffness tensors have been computed for the trabecular core of a female human lumbar vertebra (58 y) which had been scanned by µCT. Fig. 7 briefly summarizes the results in terms of a correlation plot for measured and experimental apparent stiffness for various resolutions of the image data that shows the trabecular bones. Our investigations show that there is a moderate but acceptable agreement between experiment and numerical homogenization.

5 Conclusions

We have discussed a Composite Finite Element approach to image based computing. The CFE method is capable of resolving complicated structures or interfaces on hexahedral grids as they are provided by standard voxel grids of three dimensional medical image data. In the paper we have presented possible use cases for CFE, when the domain has a complicated boundary, when an interface between different materials has complicated shape, or when the computation of efficient

macroscopic quantities, i.e., homogenization of complicated materials, is of interest. In contrast to standard FE on hexahedral grids, approximate interfaces are resolved. Thus, a higher order of convergence by CFE is expected and was verified in [20, 21, 27].

The method is based on a virtual sub-division of the hexahedral grids into tetrahedra. The CFE discretization can be implemented efficiently and a multigrid solver has been developed. The CFE implementation from [26] is open source and available as part of the QuocMesh software library [1].

We have shown the application of the CFE discretization to the simulation of radio frequency ablation in which the electric conductivity is discontinuous across a moving interface that has complicated shape. Also we demonstrate the homogenization approach for the elastic deformation of trabecular bone. As said before, for more details we refer the reader to the original publications mentioned above.

Acknowledgments. We acknowledge Martin Rumpf, Stefan Sauter, and Uwe Wolfram for their collaboration and many fruitful and inspiring discussions regarding CFE and their applications.

References

[1] AG Rumpf, Institute for Numerical Simulation, University of Bonn: Quocmesh software library, http://numod.ins.uni-bonn.de/software/quocmesh/index.html

[2] Allaire, G.: Shape optimization by the homogenization method, Applied Mathematical Sciences, vol. 146. Springer-Verlag, New York (2002)

[3] Berjano, E.J.: Theoretical modeling for radiofrequency ablation: state-of-the-art and challenges for the future. BioMedical Engineering OnLine 5:24(24) (2006)

[4] Bonito, A., DeVore, R.A., Nochetto, R.H.: Adaptive finite element methods for elliptic problems with discontinuous coefficients. SIAM J. Numer. Anal. 51(6), 3106–3134 (2013)

[5] Cazzani, A., Rovati, M.: Extrema of Young's modulus for cubic and transversely isotropic solids. Int. J. Solids Struct. 40, 1713–1744 (2003)

[6] Dick, C., Georgii, J., Westermann, R.: A real-time multigrid finite hexahedra method for elasticity simulation using CUDA. Simul. Model. Pract. Th. 19, 801–816 (2011)

[7] Efendiev, Y., Galvis, J., Hou, T.Y.: Generalized multiscale finite element methods (GMsFEM). J. Comput. Phys. 251, 116–135 (2013)

[8] Frei, S., Richter, T.: A locally modified parametric finite element method for interface problems. SIAM J. Numer. Anal. 52(5), 2315–2334 (2014)

[9] Gibson, L.J.: Biomechanics of cellular solids. J. Biomech. 38(3), 377–399 (2005)

[10] Hackbusch, W., Sauter, S.A.: Composite finite elements for the approximation of PDEs on domains with complicated micro-structures. Numer. Math. 75(4), 447–472 (1997)

[11] Harrigan, T.P., Jasty, M., Mann, R.W., Harris, W.H.: Limitations of the continuum assumption in cancellous bone. J. Biomech. 21(4), 269–275 (1988)

[12] He, Q.C., Curnier, A.: A more fundamental approach to damaged elastic stress-strain relations. Int. J. Solids Struct. 32(10), 1433–1457 (1995)

[13] Hellrung Jr., J.L., Wang, L., Sifakis, E., Teran, J.M.: A second order virtual node method for elliptic problems with interfaces and irregular domains in three dimensions. J. Comput. Phys. 231(4), 2015–2048 (2012)
[14] Hollister, S.J., Fyhrie, D.P., Jepsen, K.J., Goldstein, S.A.: Application of homogenization theory to the study of trabecular bone mechanics. J. Biomech. 24(9), 825–839 (1991)
[15] Hollister, S.J., Kikuchi, N.: A comparison of homogenization and standard mechanics analyses for periodic porous composites. Comput. Mech. 10(2), 73–95 (1992)
[16] Kröger, T., Altrogge, I., Preusser, T., Pereira, P.L., Schmidt, D., Weihusen, A., Peitgen, H.O.: Numerical simulation of radio frequency ablation with state dependent material parameters in three space dimensions. In: Larsen, R., Nielsen, M., Sporring, J. (eds.) MICCAI (2). Lecture Notes in Computer Science, vol. 4191, pp. 380–388. Springer (2006)
[17] Legrain, G., Cartraud, P., Perreard, I., Moës, N.: An X-FEM and level set computational approach for image-based modelling: Application to homogenization. Int. J. Numer. Meth. Engrg. 86(7), 915–934 (2011)
[18] Li, X., Lowengrub, J., Rätz, A., Voigt, A.: Solving PDEs in complex geometries: a diffuse domain approach. Commun. Math. Sci. 7(1), 81 (2009)
[19] Liehr, F., Preusser, T., Rumpf, M., Sauter, S., Schwen, L.O.: Composite finite elements for 3D image based computing. Comput. Vis. Sci. 12(4), 171–188 (April 2009)
[20] Pätz, T., Preusser, T.: Composite finite elements for a phase change model. SIAM J. Sci. Comput. 34(5), B672–B691 (2012)
[21] Preusser, T., Rumpf, M., Sauter, S., Schwen, L.O.: 3D composite finite elements for elliptic boundary value problems with discontinuous coefficients. SIAM J. Sci. Comput. 33(5), 2115–2143 (2011)
[22] Preusser, T., Rumpf, M., Schwen, L.O.: Finite element simulation of bone microstructures. In: Proceedings of the 14th Workshop on the Finite Element Method in Biomedical Engineering, Biomechanics and Related Fields. pp. 52–66. University of Ulm (July 2007)
[23] Rumpf, M., Schwen, L.O., Wilke, H.J., Wolfram, U.: Numerical homogenization of trabecular bone specimens using composite finite elements. In: The International Journal of Multiphysics, Special Edition: Multiphysics Simulations – Advanced Methods for Industrial Engineering. Selected Contributions from 1st Fraunhofer Multiphysics Conference. pp. 127–143 (2010)
[24] Sauter, S.A., Warnke, R.: Composite finite elements for elliptic boundary value problems with discontinuous coefficients. Computing 77(1), 29–55 (2006)
[25] Schillinger, D., Rank, E.: An unfitted *hp*-adaptive finite element method based on hierarchical B-splines for interface problems of complex geometry. Comput. Meth. Appl. Mech. Engrg. 200(47), 3358–3380 (2011)
[26] Schwen, L.O.: Composite Finite Elements for Trabecular Bone Microstructures. Ph.D. thesis, University of Bonn (2010)
[27] Schwen, L.O., Pätz, T., Preusser, T.: Composite finite element simulation of radio frequency ablation and bone elasticity. In: Eberhardsteiner, J., et al. (eds.) Proceedings of the 6th European Congress on Computational Methods in Applied Sciences and Engineering (ECCOMAS 2012). Vienna, Austria (September 2012)
[28] Schwen, L.O., Preusser, T., Rumpf, M.: Composite finite elements for 3D elasticity with discontinuous coefficients. In: Proceedings of the 16th Workshop on the Finite Element Method in Biomedical Engineering, Biomechanics and Related Fields. University of Ulm (2009)

[29] Schwen, L.O., Wolfram, U.: Validation of composite finite elements efficiently simulating elasticity of trabecular bone. Comput. Meth. Biomech. Biomed. Engrg. 17(6), 652–660 (2014)

[30] Schwen, L.O., Wolfram, U., Wilke, H.J., Rumpf, M.: Determining effective elasticity parameters of microstructured materials. In: Proceedings of the 15th Workshop on the Finite Element Method in Biomedical Engineering, Biomechanics and Related Fields. pp. 41–62. University of Ulm (July 2008)

[31] Stefan, J.: Ueber die Theorie der Eisbildung, insbesondere über die Eisbildung im Polarmeere. Ann. Phys. 42, 269–286 (1891)

[32] Stein, T.: Untersuchungen zur Dosimetrie der hochfrequenzstrominduzierten interstitiellen Thermotherapie in bipolarer Technik. Ecomed (2000)

[33] Stüben, K.: A review of algebraic multigrid. J. Comput. Appl. Math. 128(1-2), 281–309 (2001)

[34] Ün, K., Bevill, G., Keaveny, T.M.: The effects of side-artifacts on the elastic modulus of trabecular bone. J. Biomech. 39, 1955–1963 (2006)

[35] Wolfram, U., Schwen, L.O., Simon, U., Rumpf, M., Wilke, H.J.: Statistical osteoporosis models using composite finite elements: A parameter study. J. Biomech. 42(13), 2205–2209 (September 2009)

[36] Wolfram, U., Wilke, H.J., Zysset, P.K.: Rehydration of vertebral trabecular bone: Influences on its anisotropy, its stiffness and the indentation work with a view to age, gender and vertebral level. Bone 46, 348–354 (2010)